



# Numerical analysis of dynamic coupling between the keyhole and molten pool in the rotating laser welding process of aluminum alloy

Xueli Wang<sup>1</sup> · Wen Liu<sup>1</sup> · Guoxiang Xu<sup>1</sup> · Jie Zhu<sup>1</sup> · Qingxian Hu<sup>1</sup> · Baoshuai Du<sup>2</sup>

Received: 11 March 2022 / Accepted: 10 July 2022 / Published online: 18 July 2022  
© The Author(s), under exclusive licence to Springer-Verlag London Ltd., part of Springer Nature 2022

## Abstract

The stirring effect of a rotating laser on a molten pool can expand the range of the laser heat source and effectively inhibit defects such as pores and improve the quality of the weld joint. Due to laser rotation, the physical characteristics of the heat source and the dynamic behavior of the keyhole and molten pool are more complicated than those of conventional laser welding. This paper adopts a numerical simulation method. A three-dimensional model is developed, which takes into account the coupling of the keyhole, recoil pressure, and molten pool. The model can describe the dynamic behavior characteristics of keyholes and fluid flow and the formation process and mechanism of keyhole-induced pores in welds during rotating laser welding. It can be concluded that in conventional laser welding, the keyhole is deep, narrow, and unstable, which usually results in the formation of bubbles. If the bubbles in the molten pool fail to overflow in time, pores are formed. With an increase in laser rotation frequency, the keyhole becomes shallow and wide, and the dynamic behavior of the keyhole tends to be stable, which can effectively inhibit the formation of pores. When the rotating frequency is increased up to 150 Hz, the formation of pores can be completely suppressed.

**Keywords** Rotating laser · Keyhole · Fluid flow · Numerical simulation

## 1 Introduction

As an important lightweight structural material, aluminum alloy has the characteristics of low density, high specific strength, good processing and forming performance, good corrosion resistance, and low temperature performance. It is widely used in the construction of automobiles, aircraft, and high-speed trains [1–3]. However, the welding process of aluminum alloy is complex, defects such as pores are prone to occur during the welding process, and the formation process is difficult to control. Laser welding has the advantages of a fast welding speed, high power density, large weld penetration, and narrow heat-affected zone and has received attention in regard to the welding of aluminum

alloys. However, laser welding requires a high assembly accuracy of the welding workpiece, especially in the process of aluminum welding, and the weld seam is prone to welding pores. By adjusting the amplitude, frequency, and power of the laser, the size of the molten pool can be changed, and the stirring intensity of the molten pool can be adjusted. By designing the scanning path, the flow of liquid metal in the molten pool can be controlled. Aluminum alloy demonstrates potential for applications in laser welding. In recent years, a large number of experimental studies have been carried out on the weld forming mechanism of aluminum alloy laser welding. Due to the lack of existing detection equipment, the dynamic physical phenomena of the molten pool and keyhole has yet to be fully revealed. With the development of commercial computer software, numerical simulation technology has been widely used in the study of welding physical mechanisms. Therefore, to improve the reliability of the laser welding process and enhance the coupling effect of the keyhole and molten pool, the stirring effect of laser rotation on the molten pool was studied by establishing a suitable three-dimensional numerical analysis model using numerical simulation technology. The dynamic behavior and

✉ Guoxiang Xu  
xugxiang@163.com

<sup>1</sup> Key Laboratory of Advanced Welding Technology, Jiangsu University of Science and Technology, Zhenjiang, China

<sup>2</sup> State Grid Shandong Electric Power Research Institute, Jinan 250002, People's Republic of China

fluid flow characteristics of the keyhole were observed, and the mechanism of rotating laser welding was analyzed to improve the ability to suppress the welding defects of aluminum alloy and enhance the stability of welded joints. This study provides a new research and development direction for the laser welding of aluminum alloy.

Previous studies on electron beam welding demonstrated that beam oscillation has the potential to improve solidification behavior and pool geometry. These achievements guide the development of laser welding with regard to beam oscillation, which is called laser oscillating welding for simplicity [4]. Some researchers concluded that a rotating laser can stabilize the welding process and promote the formation of equiaxed crystals. They also found that circular rotation makes the weld surface smooth and results in less splashes. Cai et al. [5] concluded that scanning laser-MAG hybrid welding could efficiently suppress the porosity defects of welds. The optimal rotation frequency for porosity defect suppression was found to be 20 Hz. However, the porosity defects increased sharply with a rotation frequency of the laser over 40 Hz. Fetzer et al. [6] concluded that by applying a circular beam oscillation, the weld seams were found to be virtually free from porosity. They also found that there will be some pores in the case of laser beam welding with circular beam oscillation at 100 Hz. However, at an oscillation frequency of 200 Hz, the formation of bubbles is completely prevented. Therefore, rotating laser welding can effectively improve the welding quality under certain frequencies and rotating paths. Ke et al. [7] proposed a numerical framework of keyhole-induced porosity formation and methods to suppress porosity for laser beam oscillating welding. The wider and more stable the keyhole is, the larger and shallower the molten pool, and a more complex melt flow will decrease the possibility of keyhole collapse, inhibit bubble formation, and aid in the escape of bubbles. In addition, some other researchers also conducted simulation studies on keyhole instability and fluid flow laser or hybrid welding [8, 9], but

they did not consider the formation mechanism of keyhole-induced porosity.

According to the above review of previous studies, there is currently not much information available for the rotating laser welding of aluminum alloys under the molten pool flow mechanism. Because of the complex fluid flow and dynamic behavior of keyholes in rotating laser welding, the rotating laser welding process of aluminum alloy is difficult to directly observe and analyze through a single experiment (such as a high-speed camera observation). Therefore, with the help of a numerical simulation method, a three-dimensional transient numerical analysis model is established to simulate the rotating laser welding process of aluminum alloy. The formation mechanism of pores induced by keyholes in the rotating laser welding of aluminum alloy is studied, and the influence of frequency on this process is discussed.

## 2 Experimental procedures

Figure 1 shows sketch map of laser welding. Base metal is 6061 aluminum alloy. A continuous wave fiber laser is used, which has 6-kW peak power, 300-mm focal length and 0.3-mm focal spot diameter. Welding system is automated using an ABB 6-axis robot. Pure Ar is used as shielding gas which has a flowing rate of 22 L/min. Other welding parameters are listed in Table 1.

## 3 Model development

### 3.1 Governing equations

The gas and liquid phases are solved in the same computational domain. The fluid in the molten pool is assumed to be a Newtonian incompressible fluid. The governing equations of mass, momentum, and energy can be expressed as follows.

**Fig. 1** Schematic sketch of the laser welding process and calculation domain

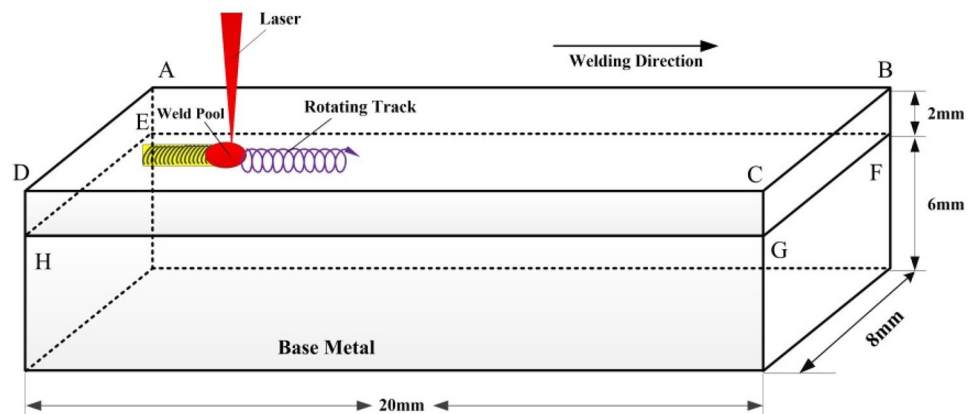


**Table 1** Process parameters in laser welding

Case	Type	Laser power (kW)	Longitudinal velocity (mm/s)	Radius of rotation (mm)	Oscillating frequency (Hz)
1	Nonrotating	5	25	0	0
2	Circular rotation	5	25	1	50
3	Circular rotation	5	25	1	100
4	Circular rotation	5	25	1	150

1. Mass

$$\frac{\partial \rho}{\partial t} + \nabla \cdot (\rho \vec{V}) = S_m \tag{1}$$

2. Momentum

$$\rho \left( \frac{\partial \vec{V}}{\partial t} + \vec{V} \cdot \nabla \vec{V} \right) = -\nabla p + \mu \nabla^2 \vec{V} - \frac{\mu \vec{V}}{K} + \rho \vec{g} \beta (T - T_{ref}) + \vec{F} \tag{2}$$

3. Energy

$$\frac{\partial(\rho H)}{\partial t} + \nabla \cdot \vec{V}(\rho H) = \nabla \cdot (k \nabla T) + S_v \tag{3}$$

where  $\rho$  is the density;  $t$  is the time;  $\vec{V}$  is the velocity;  $p$  is the pressure;  $\mu$  is the viscosity;  $K$  is the drag coefficient in the porous media;  $\vec{g}$  is the gravitational vector;  $T_{ref}$  is reference temperature;  $\beta$  is the thermal expansion coefficient;  $\vec{F}$  is the electromagnetic force vector;  $k$  is the thermal conductivity;  $T$  is the temperature;  $H$  is the enthalpy;  $S_m$  and  $S_v$  are the source terms. The third term on the right side of Eq. 2 is the source term due to the frictional dissipation in the mushy zone. The fourth term on the right side of Eq. 2 is the buoyancy force, which is calculated according to the Boussinesq approximation.

The drag coefficient is determined using the Kozeny equation, which is given by [10]:

$$K = \frac{f_l^2 d^2}{180(1 - f_l)^2} \tag{4}$$

where  $d$  is a constant on the order of  $10^{-4}$  m and  $f_l$  is the liquid fraction, which is assumed to change linearly with temperature and is defined as [11]:

$$f_l = \begin{cases} 0 & T < T_s \\ 1 & T > T_l \\ (T - T_s)/(T_l - T_s) & T_s \leq T \leq T_l \end{cases} \tag{5}$$

where  $T_s$  is the solidus temperature and  $T_l$  is the liquidus temperature. In the calculation, the enthalpy-porosity

method [8, 12] was used to consider the solid–liquid phase change, and the total enthalpy  $H$  can be calculated as

$$H = \int c_p dT + f_l L_m \tag{6}$$

where  $c_p$  is the specific heat;  $L_m$  is the latent heat of fusion; and the first and second terms on the right side represent the sensible heat and latent heat content, respectively.

In addition to heat transfer, mass transfer between liquid and gas phases also occurs due to laser-induced evaporation, which is dealt with using a simple source term in the mass continuity equation [10]:

$$S_m = \begin{cases} m_{er} \\ -m_{er} \end{cases} \tag{7}$$

where  $m_{er}$  is the evaporation rate.

### 3.2 Tracking free surface

The volume of fluid (VOF) algorithm was applied to track the free surface of the weld pool. The function  $F$  denotes the fraction of liquid in a cell, which is calculated by [13]:

$$\frac{\partial F}{\partial t} + \vec{V} \cdot \nabla F = 0 \tag{8}$$

where  $\vec{V}$  is the velocity vector. When  $F$  is 1, the cell is completely filled with molten metal; when  $F$  is 0, the cell is completely filled with air. In the case of  $0 < F < 1$ , the cell is partially filled with molten metal, which is used to determine the location of the free surface.

### 3.3 Heat source

During laser welding, a keyhole is generated due to the high density of the focused beam, which allows more laser heat to act inside the workpiece directly. For a fiber laser beam, the influence of IB absorption is minor owing to the short wavelength, and Fresnel absorption plays a dominant role due to the multiple reflections of the laser beam inside the keyhole. Several consistent keyhole models have been proposed

by some researchers [14–17], which consider the multiple Fresnel absorption of laser energy using ray tracing technology. However, these models are extremely time-consuming and involve more unknown material properties. To speed up the calculation, volumetric heat source models [18, 19] with changed peak density along the heat source height have also been established for laser density distribution. Compared with previous models [22], this kind of model can depict the distribution of laser energy more reasonably by reflecting multiple reflections indirectly. This engineering approximation has been proven to be accurate in the simulation of keyhole-induced porosity in laser welding [8, 9, 22]. In this study, a curve-rotated volumetric heat source is used to model the laser energy. The model is constructed by superimposing a number of Gaussian plane heat sources with different peak power densities and distribution parameters, and its detailed derivation process is available in Ref. [19]. The expression of the model is given by Eq. (9).

$$q_L = \frac{3\eta_L Q_L}{\pi(1 - e^{-3})(a + b)} \left[ \frac{(1 - \chi)z_i z_e}{z_i - z_e} \frac{1}{z} + \frac{\chi z_i - z_e}{z_i - z_e} \right] \exp \left\{ -\frac{3(x^2 + y^2)}{[r_0(z)]^2} \right\} \quad (9)$$

$$r_0(z) = \frac{r_e - r_i}{z_e^2 - z_i^2} z^2 + \frac{r_1 z_e^2 - r_e z_i^2}{z_e^2 - z_i^2} \quad (10)$$

where  $\eta_L$  is the laser power efficiency, which is set at 0.9;  $Q_L$  is the laser power;  $r_e$  and  $r_i$  are the radii of the top and bottom surfaces of the heat source, respectively, which are set at 1.5 mm and 1.0 mm;  $z_e$  and  $z_i$  are the z-coordinates of the top and bottom surfaces of the heat source, respectively; and the geometric parameters (i.e.,  $r_e$ ,  $r_i$ ,  $z_e$ , and  $z_i$ ) are determined according to the size of the keyhole and change with time  $t$ .  $\chi$  is the proportion coefficient between the peak power densities at the top and bottom surfaces of the heat source, which is set at 1.5. According to the work of Zhao et al. [20], the power efficiency of the laser is estimated by a simplified equation, which considers the effects of multiple reflections of the laser beam as well as IB and Fresnel absorption mechanisms. When a keyhole is formed, part of the laser volumetric heat source distributes outside the weld pool. To compensate for this part of the laser energy, the laser power efficiency is enhanced by approximately 8%.

### 3.4 Moving path of the heat source

The heat source is divided into two modes: nonrotating and rotating. Compared with nonrotating laser welding, the high-frequency rotation of the laser causes significant changes in the thermal distribution characteristics of the molten pool. Therefore, a reasonable and accurate description of the path is required. The actual movement path of the heat source center is shown in Fig. 2. The rotation path is as follows [21]:

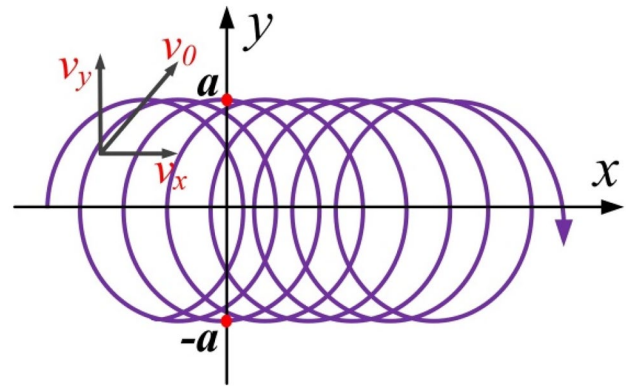


Fig. 2 Schematic diagram of the rotation path

$$\begin{cases} x(t) = x_0 + v_0 t + a \cdot \cos(2\pi \cdot f \cdot t) \\ y(t) = a \cdot \sin(2\pi \cdot f \cdot t) \end{cases} \quad (11)$$

where  $a$  is the radius of laser rotation, which is set at 1;  $f$  is the rotation frequency; and  $x_0$  is the position of the laser rotation center on the  $x$ -axis.

### 3.5 Boundary conditions

As observed in Fig. 1, the boundary ABCD is set as the pressure outlet, and the other boundaries are set as the walls. The following conditions should be satisfied:

$$P_{\text{outlet}} = P_0 \quad (12)$$

$$T_{\text{outlet}} = T_0 \quad (13)$$

where  $P_0$  and  $T_0$  mean the ambient pressure and temperature during welding.

The energy transfer equation is described as

$$-k\partial T/\partial n = q_{\text{laser}} - q_e - q_r - q_c \quad (14)$$

where  $q_{\text{laser}}$  is the laser heat input, and  $q_e$ ,  $q_r$ , and  $q_c$  represent the heat losses due to convection, radiation, and evaporation, respectively. They are expressed as follows.

$$q_e = \alpha(T - T_0) \quad (15)$$

$$q_r = \varepsilon\sigma(T^4 - T_0^4) \quad (16)$$

$$q_c = m_c L_c \quad (17)$$

where  $\alpha$  is the convection heat transfer coefficient;  $\varepsilon$  is the surface radiation emissivity;  $\sigma$  is the Stefan-Boltzmann constant;  $m_c$  is the evaporation;  $L_c$  is the latent heat of evaporation; and  $T_0$  is the ambient temperature.

In laser welding, the keyhole has a strong stirring influence on the fluid in the weld pool, so it will affect the dynamic behavior of the molten pool. The keyhole is regarded as the surface deformation of the molten pool under the combined action of laser-induced steam reaction force and surface tension. The pressure boundary condition along the normal direction of the free surface is given as:

$$P = P_R - P_S + 2\mu \frac{\partial V_s}{\partial s} \tag{18}$$

where  $P_R$  is the recoil pressure and  $P_S$  is the surface tension.

The equation for recoil pressure is given as follows [13]:

$$P_r = 0.54P_0 \exp [L_h(T - T_b)/(RTT_b)] \tag{19}$$

where  $P_0$  is the atmospheric pressure;  $L_h$  is the latent heat of evaporation;  $R$  is the universal gas calculation constant;  $T$  is the temperature of the weld pool free surface; and  $T_b$  is the boiling temperature of the aluminum.

The surface tension can be expressed as

$$P_S = \kappa\gamma \tag{20}$$

where  $\kappa$  is the free surface curvature and  $\gamma$  is the surface tension coefficient.

The Maragani shear stress on the molten pool surface is tangent to the free surface, which is estimated by the following analytical solution:

$$\mu_s \frac{\partial V_s}{\partial s} = - \frac{\partial \gamma}{\partial T} \frac{\partial T}{\partial s} \tag{21}$$

where  $V_s$  is the tangential component of the velocity and  $s$  is the tangential vector of the local surface.

### 3.6 Calculation method

The molten pool of the rotating laser welding process was simulated by FLUENT. Because the gas–liquid and gas–solid interfaces are located in the interior of the calculation region, the boundary conditions for the interface of the two phases are treated as volume terms in the governing equations according to the method proposed by Brackbill et al. [22]. A pressure-implicit operator split (PISO) scheme is utilized to perform the coupling of the temperature and velocity fields. To take into account the calculation accuracy and efficiency, a non-uniform grid system is used for calculation and simplification, and hexahedral mesh generation is adopted, as shown in Fig. 3, and a variable time step method is used for simulation calculation. The minimum grid size is 0.1 mm, and the total number of grids is 211,200. The time step is between  $10^{-5}$  and  $10^{-6}$  s. The thermal properties and other parameters used in the calculation are shown in Table 2.

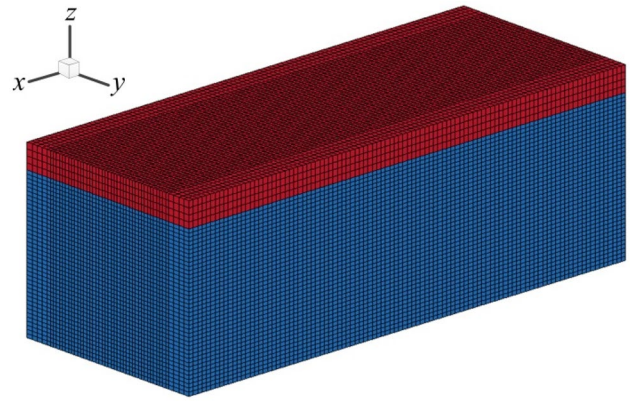


Fig. 3 Mesh generation of geometric model

## 4 Results and discussions

### 4.1 Conventional laser welding process

Figure 4 shows the main process of keyhole-collapse-bubble formation in conventional (nonrotating) laser welding. The workpiece begins to melt, and the most obvious feature of laser welding appears, i.e., the keyhole, as shown in Fig. 4a. When the keyhole reaches its maximum depth, the wall of the keyhole folds and is unstable, as shown in Fig. 4b. Figure 4c shows that the keyhole collapses, causing air or protective gas to enter the molten pool and form bubbles. If the keyhole collapses again, bubbles are formed again (Fig. 4d). This is consistent with the morphology of the keyhole observed by Wu et al. [26] using high-speed photography, as shown in Fig. 5.

Table 2 Thermophysical properties and other parameters used in the calculation [23–25]

Material properties	Value
Density of aluminum alloy, $\rho$	2630 kgm <sup>-3</sup>
Dynamic viscosity of liquid phase, $\mu$	0.0013 kgm <sup>-3</sup> s <sup>-1</sup>
Thermal conductivity of solid phase, $k_s$	220 Wm <sup>-1</sup> K <sup>-1</sup>
Thermal conductivity of liquid phase, $k_l$	140 Wm <sup>-1</sup> K <sup>-1</sup>
Specific heat of liquid phase, $c_{pl}$	1200 Jkg <sup>-1</sup> K <sup>-1</sup>
Specific heat of solid phase, $c_{ps}$	900 Jkg <sup>-1</sup> K <sup>-1</sup>
Latent heat of fusion, $L_m$	$3.97 \times 10^5$ Jkg <sup>-1</sup>
Latent heat of evaporation, $L_c$	$1.05 \times 10^7$ Jkg <sup>-1</sup>
Thermal expansion, $\beta$	$2.36 \times 10^{-5}$ K <sup>-1</sup>
Solidus temperature, $T_s$	858 K
Liquidus temperature, $T_l$	930 K
Ambient temperature, $T_0$	295 K
Surface radiation emissivity, $\epsilon$	0.4
Stefan-Boltzmann constant, $\sigma$	$5.57 \times 10^{-8}$ Wm <sup>-2</sup> K <sup>-4</sup>
Convective heat transfer coefficient, $\alpha_c$	80 Wm <sup>-1</sup> K <sup>-1</sup>
Surface tension coefficient, $\gamma$	1.2 Nm <sup>-1</sup>

## 4.2 Dynamic behavior of the weld pool in rotating laser welding

Figure 6 shows iso-surfaces of weld pool in rotating laser welding at different times. To further explain the mechanism of the inhibition process, the main process of the rotating laser inhibiting pores in a certain period has been shown in Figs. 7 and 8. Figure 7a shows that when  $t=0.0894$  s, the laser is located at position B. Under the recoil pressure and the rotation of the keyhole, the liquid metal in the front wall of the keyhole flows upward and transversely, and the maximum flow velocity of the molten pool is 2.72 m/s. Under the action of the recoil pressure and surface tension, the liquid metal on the back side of the keyhole flows backward along the upper surface of the molten pool and forms a counterclockwise vortex in the middle of and behind the molten pool. The liquid metal in the middle of the molten pool flows to the keyhole. Figure 7b shows that due to the eddy current in the molten pool and under the action of the dynamic pressure of the molten pool, the back wall of the keyhole is unstable and collapses, so bubbles are formed below the keyhole. Meanwhile, Fig. 7c shows that when  $t=0.0918$  s, the laser is located between positions B and C, and the hole changes with the laser rotation position and disappears in this section. When the laser rotates to position D, the keyhole is above the pores, as shown in Fig. 7d.

**Fig. 4** Process of porosity formation in non-rotating laser welding

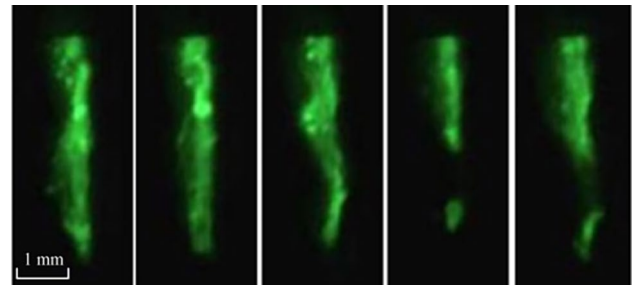
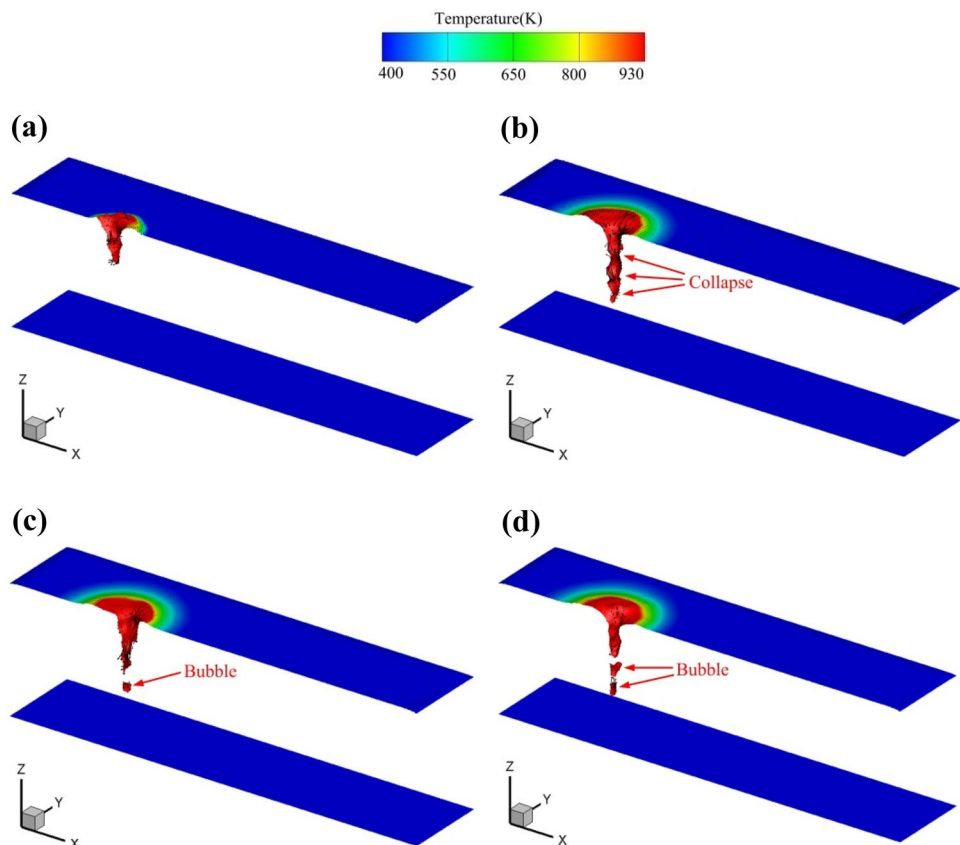
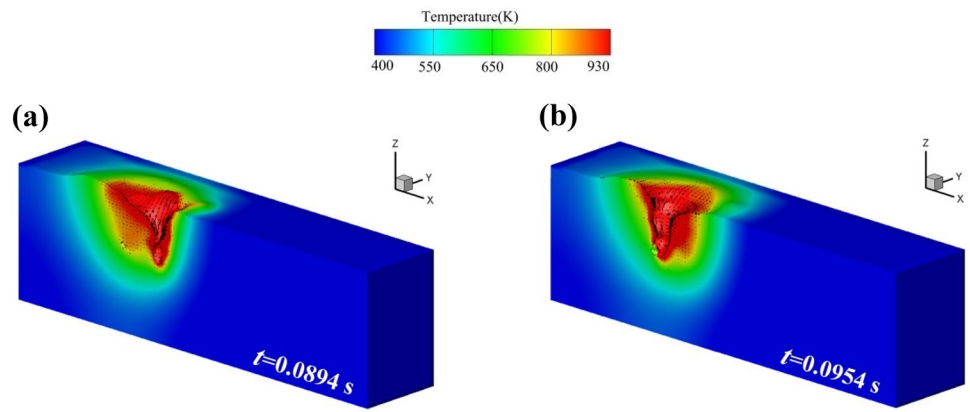


**Fig. 5** Keyhole detection image of laser welding [26]

Under the action of recoil pressure, the liquid metal near the keyhole wall flows upward rapidly, with a maximum flow rate of 2.18 m/s. Until  $t=0.0954$  s, pores were captured by keyhole. Under the action of the eddy current and dynamic pressure in the front molten pool, liquid metal will backfill the keyhole. The gas in the pores is discharged with the keyhole, and when  $t=0.1102$  s, the gas completely overflows the molten pool, and the keyhole rotates between D and A, as shown in Fig. 7e–g. The above process is consistent with the results from the high-speed camera observations taken by Fetzer et al. [6] when studying the pore inhibition mechanism, further validating the reasonability of the built model. However, it is impossible to ensure that all pores or bubbles can be captured and completely overflow by the action of

**Fig. 6** Iso-surfaces of process of the rotating laser inhibiting pores



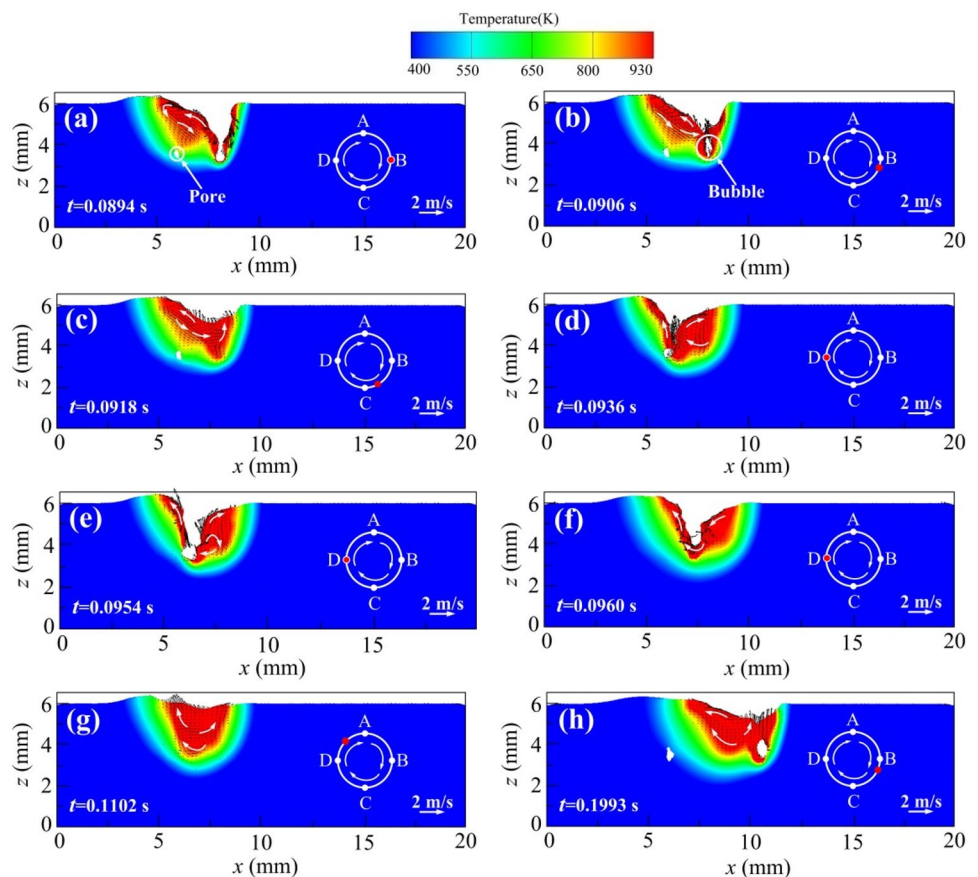
the rotating keyhole. As shown in Fig. 7h, at  $t=0.1993s$ , there is a pore behind the molten pool. With the progression of the welding process, the bubbles move with the rotation and forward movement of the laser. In the effective overlap range of the laser, the pores or bubbles have the opportunity to be captured and overflow. If not, they will be captured by the condensed metal to form pores. In addition, bubbles also move horizontally with the flow of liquid metal, as shown in Fig. 8.

As shown in Fig. 8a, at  $t=0.0750 s$ , the laser rotates to position A, and the hole depth is 2.85 mm. A clockwise vortex appears in the molten pool on the right side of the

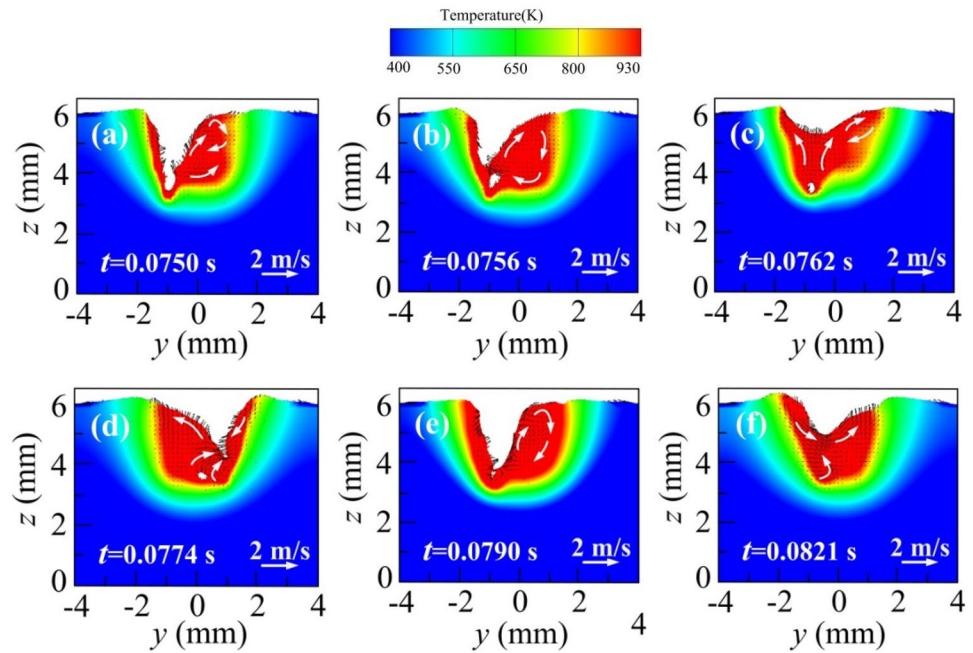
keyhole. The liquid metal flow in the molten pool near the keyhole wall is faster, and the maximum flow rate is 3.5 m/s. Figure 8b depicts the keyhole wall collapsing and forming bubbles. When the laser is near position C, as shown in Fig. 8d, the bubbles move to the middle of the molten pool with the lateral flow of the liquid metal at the bottom of the molten pool. As shown in Fig. 8e, at  $t=0.0790 s$ , the laser rotates again to position A, and the holes combine with the bubbles. Until  $t=0.0821 s$ , the gas in the bubble completely overflows with the pores, as shown in Fig. 8f.

Figure 9 shows the iso-surfaces when the rotation frequencies are 100 Hz and 150 Hz, respectively. When the

**Fig. 7** Process of the rotating laser inhibiting pores;  $Q_L=5 kW$  and  $f=50 Hz$ . A, B, C, and D represent the position of a period when the laser moves from the upper surface of the workpiece



**Fig. 8** Process of the rotating laser inhibiting pores in the cross section;  $Q_L=5$  kW and  $f=50$  Hz



rotating frequency increases to 100 Hz, the flow state of the molten pool is similar to that of the rotating frequency of 50 Hz. The liquid metal near the keyhole wall flows upward under the action of the recoil pressure. At the same time, the eddy current is formed in the rear molten pool due to the surface tension. Due to the increase in rotation frequency, the depth of the keyhole decreases, and the effect of the keyhole stirring increases the transverse flow trend of the molten pool, which reduces the velocity of the liquid metal flowing upward along the keyhole wall, and the keyhole is more stable, as shown in Fig. 10a. In Fig. 10b, it is shown that the molten pool does not form bubbles when the laser leaves position A, which is also due to the high-speed transverse flow of the liquid metal. The closer the liquid metal is to the upper part of the keyhole, the greater the flow velocity, which is because the upper temperature gradient of the molten pool is larger,

the surface tension driven by the temperature gradient is larger, and the keyhole wall is more stable. In addition, it can also be observed that the opening diameter of the keyhole increases significantly, so the keyhole is more stable.

Compared with the rotation frequencies of 50 Hz and 100 Hz, when the laser rotation frequency increases to 150 Hz, the opening diameter of the keyhole is the largest. The liquid metal near the front wall of the keyhole flows downward under the dynamic pressure of the molten pool, and the molten pool near the back wall of the keyhole flows backward under the action of the surface tension. The maximum flow rate is 3.93 m/s. Therefore, the opening diameter of the keyhole is larger, and its depth is smaller, as shown in Fig. 10c, d. Based on the above, it can be concluded that the keyhole wall does not easily collapse. Therefore, the generation of bubbles in the molten pool is prevented, and the formation of pores can be effectively inhibited.

**Fig. 9** Iso-surfaces at different rotational frequencies

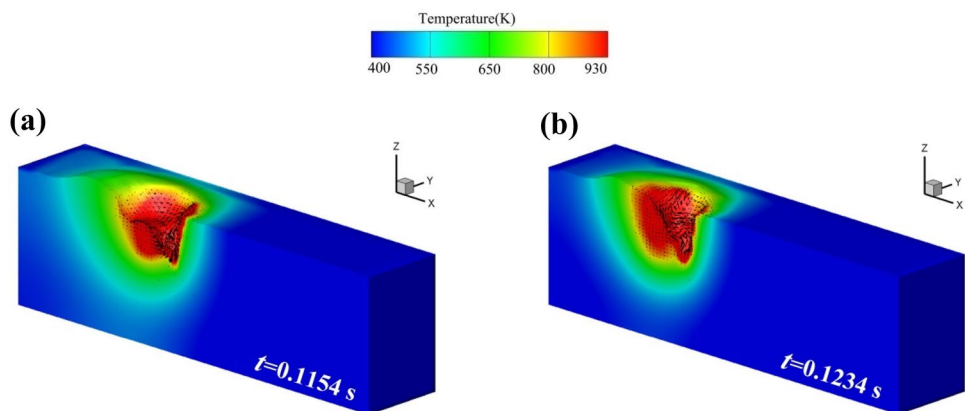
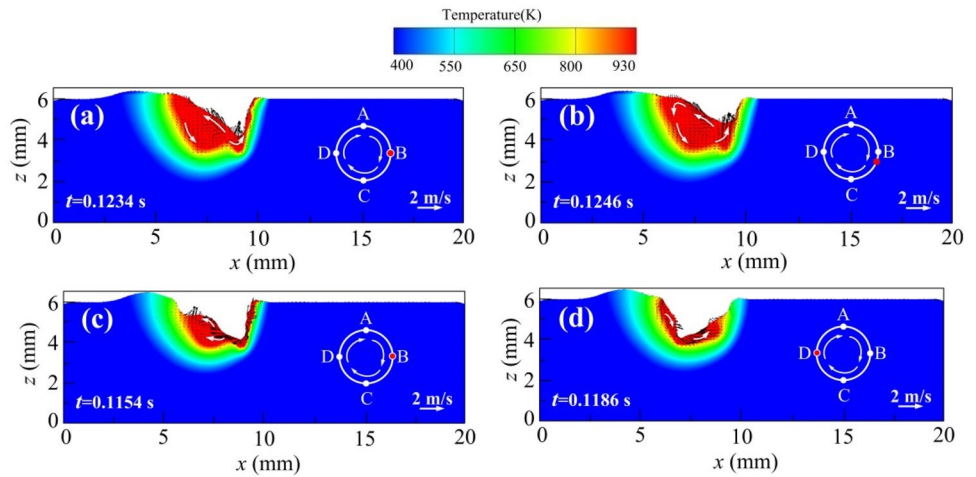




**Fig. 10** Temperature and velocity field distribution of the longitudinal section in the molten pool center; **a–b**  $QL=5$  kW and  $f=100$  Hz; **c–d**  $QL=5$  kW and  $f=150$  Hz

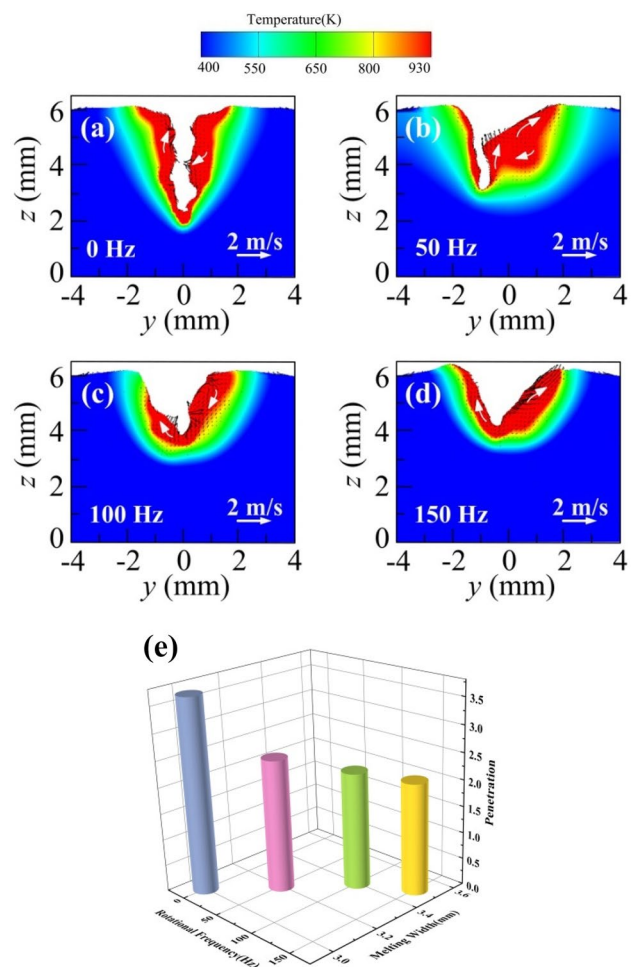


### 4.3 Effect of rotation frequency on weld topography

Figure 11 depicts the effect of the rotation frequency on the cross-section topography of the weld. It can be observed that at the same laser power, the penetration depth of conventional laser welding is the largest, the width is the smallest, and the keyhole is narrow and deep. With increasing rotation frequency, the laser energy disperses, and the depth of the molten pool decreases. The transverse (X–Y) flow velocity of the liquid metal increases, and the transverse energy transfer is promoted under the rotating stirring of the keyhole, so the width of the molten pool increases. It can also be observed that with increasing frequency, the keyhole depth decreases, and the opening diameter of the keyhole increases significantly. Figure 11e shows the influence of the rotation frequency on the width and depth of the molten pool. The change in depth is not obvious at frequencies of 100 Hz and 150 Hz because when the frequency is high, the laser energy superposition effect occurs between the laser rotation process and the previous cycles, which increases the heat input. Therefore, even if the time at the same position is shortened, the heat input is supplemented.

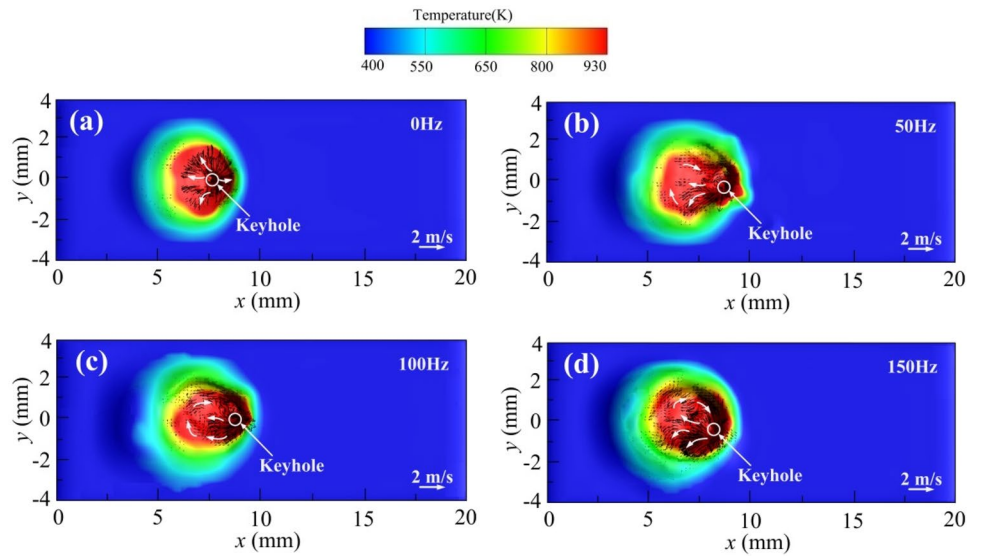
Figure 12 shows the temperature and velocity distributions of the upper surface of the molten pool at different frequencies. The molten pool of conventional laser welding is axisymmetric from the upper surface, as shown in Fig. 12a. With the laser moving forward at high speed, the front of the molten pool has a preheating effect on the base metal, and there is heat accumulation in the rear of the molten pool. Therefore, the temperature gradient in the front of the keyhole is larger than that in the rear, and the area of the rear molten pool is larger than that in the front. Driven by the surface tension and temperature gradient, the liquid metal flows to the rear of the molten pool, so the molten pool is oval with a trailing shape. When the rotation frequency is 50 Hz or 100 Hz, the molten pool is stirred by laser rotation, and the flow state of the liquid metal is more complex.

Under the action of laser stirring and the surface tension of the molten pool, a counterclockwise eddy current is formed in front of the keyhole, and it is obvious that the molten pool is asymmetric, as shown in Fig. 12b, c. Figure 12d shows



**Fig. 11** Effect of the rotating frequency on the cross-section topography and average width and depth of the molten pool

**Fig. 12** Temperature and velocity field distribution on the upper surface of the molten pool;  $Q_L=5$  kW



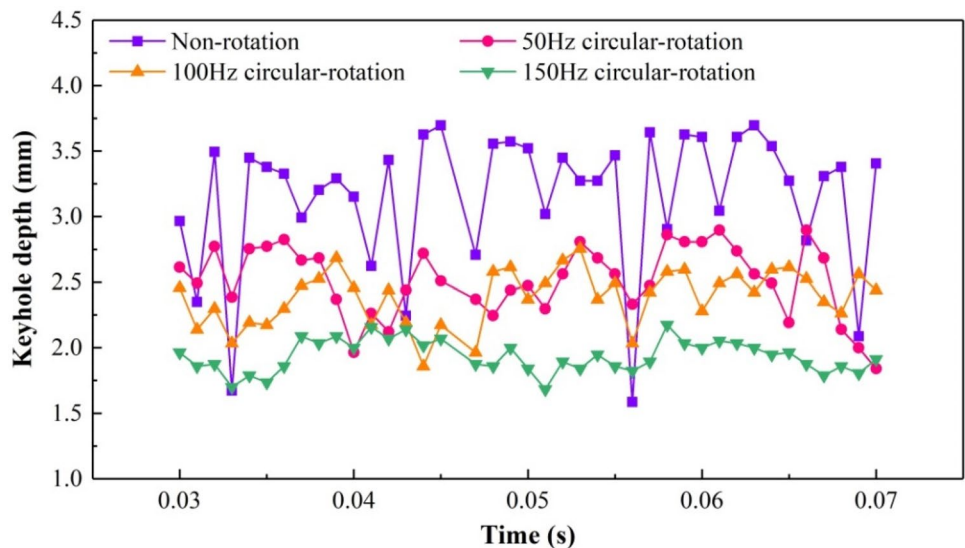
that when the rotation frequency is 150 Hz, due to the high-speed rotation of the laser, the high-speed flow of the liquid metal, and the overlap of laser energy in the welding process, it is difficult to cool the molten pool area, so the temperature gradient of the molten pool is small, and the morphology is round.

Figure 13 depicts the evolution of pore depth over time at different rotating frequencies. It can be observed that the keyhole depth curve without rotation has the largest fluctuation, indicating that the collapse of keyhole occurs at the middle part more often. In addition, when the laser beam rotates, the curve becomes smoother with the increase of laser frequency, especially at 150 Hz. This is because with the increase of rotation frequency, the depth of the keyhole decreases as a whole and the opening diameter increases.

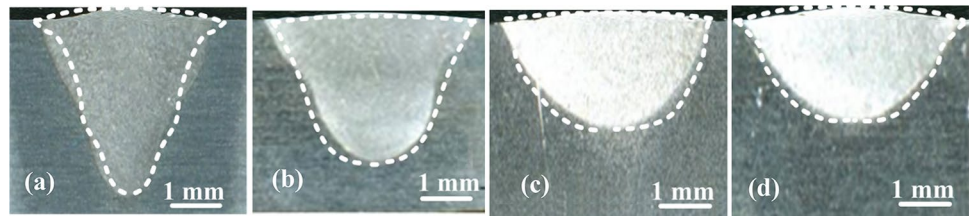
Therefore, the change of keyhole depth is relatively stable. It means that the stability of the keyhole increases and it is not easy to collapse and produce bubbles, which effectively inhibits the formation of pores.

Figure 14 compares the calculated results of weld geometries and dimensions with the experimental ones for different welding conditions. It is indicated that the simulated results are in general agreement with the measured ones, further validating the reasonability of the established model. Also, there is still some discrepancy between the calculated and the experimental weld bead geometry. This is mainly due to the insufficiency in the high temperature properties of materials as well as the simplifications of some sub-models, which will be solved in the future work.

**Fig. 13** Evolution of keyhole depth



**Fig. 14** Comparison of the calculated and experimental weld geometries and sizes; **a**  $f=0$  Hz, **b**  $f=50$  Hz, **c**  $f=100$  Hz **d**  $f=150$  Hz; white lines represent the calculated data



## 5 Conclusions

1. Compared with conventional laser welding, rotating laser welding has a strong stirring effect on the molten pool, and with an increase in the rotating frequency, the stirring effect is more obvious, which increases the transverse flow of the molten pool and increases the weld width. The time of laser action at the same position decreases, and the penetration decreases.
2. The upper surface of the conventional laser welding pool is symmetrically distributed. When the laser is rotated, it is obviously asymmetric. Due to the stirring effect of the keyhole and the surface tension, an eddy current is generated on the surface of the molten pool, which increases the complexity of the liquid metal flow.
3. Due to the laser rotation, the dynamic behavior of keyhole is more complex. The depth of the keyhole decreases, the opening diameter of the keyhole increases, and the stability increases. The keyhole can be rotated to combine with bubbles or pores, and the gas can be discharged with the keyhole. Therefore, it has an inhibitory effect on the generation of pores.
4. With the increase of laser rotation frequency, the depth of the keyhole is further decreased, and the diameter of the opening is further increased. The keyhole is more stable and resists collapse, which can effectively reduce the generation of pores. When the frequency increases to 150 Hz, the keyhole hardly collapse to form bubbles, and the pores can be effectively suppressed.

**Author contribution** All authors contributed to the study conception and design. Material preparation, data collection, and analysis were performed by JZ, QH, and BD. GX and WL developed the model. The first draft of the manuscript was written by XW, and all authors commented on previous versions of the manuscript. All authors read and approved the final manuscript.

**Funding** This research is financially supported by the National Natural Science Foundation of China (Grant No. 51975263).

## Declarations

**Conflict of interest** The authors declare no competing interests.

## References

1. Dursun T, Soutis C (2014) Recent developments in advanced aircraft aluminum alloys. *Mater Des* 56:862–871. <https://doi.org/10.1016/j.matdes.2013.12.002>
2. Schubert E, Klassen M, Zerner I, Walz C, Sepold G (2001) Light-weight structures produced by laser beam joining for future applications in automobile and aerospace industry. *J Mater Process Technol* 115:2–8. [https://doi.org/10.1016/S0924-0136\(01\)00756-7](https://doi.org/10.1016/S0924-0136(01)00756-7)
3. Miller WS, Zhuang L, Bottema J, Wittebrood AJ, De Smet P, Haszler A, Vieregge A (2000) Recent development in aluminum alloys for the automotive industry. *Mater Sci Technol* 280:37–49. [https://doi.org/10.1016/S0921-5093\(99\)00653-X](https://doi.org/10.1016/S0921-5093(99)00653-X)
4. Wang L, Gao M, Zhang C, Zeng XY (2016) Effect of beam oscillating pattern on weld characterization of laser welding of AA6061-T6 aluminum alloy. *Mater Des* 108:707–717. <https://doi.org/10.1016/j.matdes.2016.07.053>
5. Cai C, Li L, Tao W, Chen X (2016) Effects of weaving laser on scanning laser-MAG hybrid welding characteristics of high-strength steel. *Sci Technol Weld Joining* 12:104–109. <https://doi.org/10.1080/13621718.2016.1199126>
6. Fetzer F, Sommer M, Weber R, Weberpals J, Graf T (2018) Reduction of pores by means of laser beam oscillation during remote welding of AlMgSi. *Opt Lasers Eng* 49:68–77. <https://doi.org/10.1016/j.optlaseng.2018.04.012>
7. Ke WC, Bu XZ, Oliveira JP, Xu WG, Wang ZM, Zeng Z (2021) Modeling and numerical study of keyhole-induced porosity formation in laser beam oscillating welding of 5A06 aluminum alloy. *Opt Laser Technol* 133:106540. <https://doi.org/10.1016/j.optlastec.2020.106540>
8. Xu GX, Li PF, Cao QN, Hu QX, Gu XY, Du BS (2018) Modeling of fluid flow phenomenon in laser-GMAW hybrid welding of aluminum alloy considering three phase coupling and arc plasma shear stress. *Opt Laser Technol* 100:244–255. <https://doi.org/10.1016/j.optlastec.2017.10.009>
9. Xu GX, Zhang WW, Liu P, Du DS (2015) Numerical analysis of fluid flow in laser-GMAW hybrid welding. *Acta Metall Sin* 51:713–723. <https://doi.org/10.11900/0412.1961.2014.00464>
10. Li XB, Lu FG, Cui HC, Tang XH, Wu YX (2014) Numerical modeling on the formation process of keyhole-induced porosity for laser welding steel with T-joint. *Int J Adv Manuf Technol* 72:241–254. <https://doi.org/10.1007/s00170-014-5609-x>
11. Kumar A, Debroy T (2007) Heat transfer and fluid flow during gas-metal-arc fillet welding for various joint configurations and welding positions. *Metall Mater Trans A* 38:506–519. <https://doi.org/10.1007/s11661-006-9083-4>
12. Wu CS, Zhang TH, Chen J (2017) Numerical simulation of keyhole behaviors and fluid dynamics in laser-gas metal arc hybrid welding of ferrite stainless steel plates. *J Manuf Process* 25:235–245. <https://doi.org/10.1016/j.jmapro.2016.11.009>
13. Cho JH, Na SJ (2009) Three-dimensional analysis of molten pool in GMA-laser hybrid welding. *Weld J* 88:35–43

14. Cho WI, Na SJ, Cho MH, Lee SJ (2010) Numerical study of alloying element distribution in CO<sub>2</sub>laser-GMA hybrid welding. *Comput Mater Sci* 49:49–53. <https://doi.org/10.1016/j.commatsci.2010.06.025>
15. Pang SY, Chen WD, Wang W (2014) A quantitative model of keyhole instability induced porosity in laser welding of titanium alloy. *Metall Mater Trans A* 45:2808–2818. <https://doi.org/10.1007/s11661-014-2231-3>
16. Pang SY, Chen X, Zhou JX, Shao XY, Wang CM (2015) 3D transient multiphase model for keyhole, vapor plume, and weld pool dynamics in laser welding including the ambient pressure effect. *Opt Lasers Eng* 74:47–58. <https://doi.org/10.1016/j.optlaseng.2015.05.003>
17. Cho JH, Na SJ (2006) Implementation of real-time multiple reflection and Fresnel absorption of laser beam in keyhole. *J Phys D Appl Phys* 39:5372–5378. <https://doi.org/10.1088/0022-3727/39/24/039>
18. Xu GX, Pan HC, Liu P, Li PF, Hu QX, Du BS (2018) Finite element analysis of residual stress in hybrid laser-arc welding for butt joint of 12 mm-thick steel plate. *Welding in the World* 63:289–300. <https://doi.org/10.1007/s40194-017-0545-7>
19. Xu GX, Wu CS, Qin GL, Wang XY, Lin SY (2011) Adaptive volumetric heat source models for laser beam and laser-pulsed GMAW hybrid welding processes. *Int J Adv Manuf Technol* 57:245–255. <https://doi.org/10.1007/s00170-011-3274-x>
20. Zhao H, Niu W, Zhang B, Lei Y, Kodama M, Ishide T (2011) Modelling of keyhole dynamics and porosity formation considering the adaptive keyhole shape and three-phase coupling during deep-penetration laser welding. *J Phys D Appl Phys* 44:485302. <https://doi.org/10.1088/0022-3727/44/48/485302>
21. Hugger F, Hofmann K, Kohl S, Dobler M, Schmidt M (2015) Spatter formation in laser beam welding using laser beam oscillation. *Weld World* 59:165–172. <https://doi.org/10.1007/s40194-014-0189-9>
22. Brackbill JU, Kothe DB, Zemach C (1992) A continuum method for modeling surface tension. *J Comput Phys* 100:335–354. [https://doi.org/10.1016/0021-9991\(92\)90240-Y](https://doi.org/10.1016/0021-9991(92)90240-Y)
23. Zhou J, Tsai HL (2007) Effects of electromagnetic force on melt flow and porosity prevention in pulsed laser keyhole welding. *Int J Heat Mass Transf* 50:2217–2235. <https://doi.org/10.1016/j.ijheatmasstransfer.2006.10.040>
24. Xu GX, Zheng ZQ, Cao QN, Hu QX, Li L, Guo QH, Du BS (2019) Numerical and experimental investigation on weld formation during laser+MIG hybrid fillet welding of aluminum alloy in horizontal position. *Int J Adv Manuf Technol* 102:2683–2694. <https://doi.org/10.1007/s00170-019-03372-3>
25. Pang SY, Chen WD, Zhou JX, Liao DM (2015) Self-consistent modeling of keyhole and weld pool dynamics in tandem dual beam laser welding of aluminum alloy. *J Mater Process Technol* 217:131–143. <https://doi.org/10.1016/j.jmatprotec.2014.11.013>
26. Wu Q, Xiao RS, Zou JL, Xu JJ (2018) Weld formation mechanism during fiber laser welding of aluminum alloys with focus rotation and vertical oscillation. *J Manuf Process* 36:149–154. <https://doi.org/10.1016/j.jmapro.2018.10.004>

**Publisher's Note** Springer Nature remains neutral with regard to jurisdictional claims in published maps and institutional affiliations.